Science Advances
AAAS

advances.sciencemag.org/cgi/content/full/7/20/eabd1505/DC1

# Supplementary Materials for

## Noninvasive visualization of electrical conductivity in tissues at the micrometer scale

Yuanhui Huang, Murad Omar, Weili Tian, Hernán Lopez-Schier, Gil Gregor Westmeyer, Andriy Chmyrov,
George Sergiadis, Vasilis Ntziachristos*

*Corresponding author. Email: v.ntziachristos@tum.de

Published 12 May 2021, *Sci. Adv.* **7**, eabd1505 (2021)
DOI: 10.1126/sciadv.abd1505

**The PDF file includes:**

Notes S1 to S6
Table S1
Figs. S1 to S5
Legends for movies S1 to S3
References

**Other Supplementary Material for this manuscript includes the following:**

(available at advances.sciencemag.org/cgi/content/full/7/20/eabd1505/DC1)

Movies S1 to S3

# Supplementary Text

## Note S1. RF field distribution / homogeneity and coupling in RThAM

To test our assumption of a homogeneous electric field in the TxLine, we performed simulation studies (see Materials and Methods) of the RF field distribution at 300 MHz using commercial EM simulation software (CST studio), with and without a sample present. Figure S1D shows the result without sample, and fig. S1E shows that with a water-rich sample installed (spherical egg with permittivity of 80.1 and conductivity 1 S/m). Less than 3 dB in E-field inhomogeneity is observed inside the water sample and therefore we assumed the E-field is homogeneous inside aqueous samples. For lower frequencies, the field is expected to be more homogeneous than the simulation. This simulation supported the validity of our choice of an open TxLine for near-field coupling and represented one of the key advantages of this RF coupling method (confirmed with suture in fig. S3, A and B). Compared to other coupling methods (*32, 35–37*), the open TxLine is capable of homogeneously 'concentrating' the pulsed RF energy in a tight 3D space between the two conductor plates. Therefore, for spherical absorbers such homogeneous field distribution in sample chamber would yield homogeneous contrast in RThAM 3D FOV.

We evaluate the coupling efficiency of RF energy to the antenna by the percentage of power that is transmitted through open transmission line and finally absorbed by the 50-ohm terminator. Figure S1C shows the voltage standing wave ratio (VSWR) measured at the input to TxLine with a vector network analyzer (VNA Master MS2036A, Anritsu). The VSWR at 300 MHz of 1.36 indicates >97% power transmission. The pulse energy of our RF pulser $E_{pulse} = V_p^2 / Z_0 \times \tau = (10 \times 10^3 \text{ volt})^2 / 50 \text{ Ohm} \times 1.5 \times 10^{-9}$ second $= 3 \times 10^{-3}$ J, which is 3 mJ. Here $V_p$ is the peak voltage, $Z_0$ the resistance of RF load, $\tau$ the pulse width. As a result, this design of open TxLine enabled RF energy coupling of $0.97 \times 3$ mJ $= 2.91$ mJ was coupled through a cross-section of $1 \times 3$ mm$^2$ of TxLine, laying down the foundation to high SNR RThAM signal generation.

The coupling efficiency from open transmission line to tissue, which is in fact the thermoacoustic generation efficiency, can be estimated by the conductivity ($\sigma$) loss via Joule heating: $H_0 = \sigma|E|^2$ where $E$ is the electric field strength in dielectric medium that reduces the strength of external electric field by a factor of the dielectric constant $\varepsilon_r$ [Chapter 10. Dielectrics, Feynman Lectures on Physics Volume II (*56*)]. Here we applied a simplified electrostatic analysis because we considered the dielectric relaxation of polar molecules to be instantaneous [for water (*40*) the relaxation time is 1.1 ps at 298 K].

## Note S2. Coupling media for RF energy and US wave

Table S1 summarizes the theoretical RF field strength decrease and US attenuations in different coupling modes of RThAM using the same open transmission line, with the same dielectric gap, and assuming ideal impedance matching to 50 ohm. We have shown the simulation results in fig. S1 (D to E) to show the electric field strengths in oil and in aqueous egg sample. Inspecting the field strength relative to the peak in the cross-sectional plane shows a decrease of -37 dB at the sample center and -14 dB in the oil region that is undisturbed by the sample. Thus, the simulated field strengths indeed are close to the predicted values, shown in table S1 (obtained by a simplified theoretical analysis considering only the polarization field effect). We note that the difference in the simulated field strengths between the oil and aqueous samples (23 dB) is lower than the predicted difference of 30.29 dB (table S1). However, this difference between the simplified theoretical prediction and simulation does not change the conclusion of table S1 — hybrid coupling is better than either pure oil or pure water coupling in our scenario considering both RF field and US coupling. For finer predictions, we believe it would be necessary to carry out more detailed modeling, for example by considering the local fields at the conductors' edges, sample properties, imperfections in engineering, etc.

Because the mechanism of RF-induced thermoacoustic generation ($p_0 \approx \Gamma\sigma|E|^2$) relies on the E-field strength to generate detectable thermoacoustic signals, our energy coupling strategy is to maximize the electric field strength ($E$) established in the coupling medium that supports the sample, as allowed by the output voltage of our pulser and the limiting electric breakdown voltage of the medium. Only impedance matching does not satisfy the requirement and we need to further optimize the portion of energy/strength in the form of electric field relative to magnetic field. However, to combine RF field excitation and US wave detection for high resolution RThAM imaging, one of the challenges lies in coupling the RF field and US wave. Usually, a couplant that is efficient to deliver electric field energy is suboptimal for US wave coupling. For example, if we optimized for US wave coupling, and used de-ionized water as a dielectrics for the open TxLine, the delivered RF field would be a result of the external electric field minus the polarized electric field in water, which results in an RF field that is reduced by the dielectric constant of water, $\varepsilon_r = 80.1$ at 293 K. That is the case in the copper wire characterization experiments (Fig. 1 and fig. S2). We chose de-ionized water as the dielectric to fill the TxLine (dielectric gap 6 mm) in order to optimize for US coupling and biological experiments. This water-filled TxLine has characteristic impedance of 25 ohm and matched with two 25-ohm RF resistors before and after it. It is not 50 ohm because a 50 ohm line will have unrealistic dielectric gap of 110 mm. Since the RThAM generation of copper is strong, this energy coupling element is sufficient. But such TxLine design was found experimentally insufficient to excite detectable RThAM signal from biological tissue. Instead, we chose oil as dielectrics to fill TxLine because of its low dielectric constant (negligible polarization E-field) which gives us in return shorter dielectric gap (1 mm, see Materials and Methods) than a 25-ohm TxLine using de-ionized water, and therefore higher electric field strength and desirable energy flux delivered to sample. But oil-filled TxLine brings challenge in US wave coupling.

Due to viscosity of oil (30 cSt for mineral oil, same for kitchen oil) and low speed of sound (SoS; 900 m/s), oil attenuates US wave strongly. According to Stokes' law of acoustic attenuation, we calculated and showed in fig. S1F the US attenuation in mineral oil (viscosity 30 cSt; specific gravity 870 kg/m$^3$; SoS 985 m/s; M8410, Sigma Aldrich), silicone oil of 2 cSt (viscosity 2 cSt; specific gravity 872 kg/m$^3$; SoS 931 m/s; PSF-2cSt, Clearco Products), silicone oil of 0.65 cSt (viscosity 0.65 cSt; specific gravity 760 kg/m$^3$; SoS 891 m/s; PSF-0.65cSt, Clearco Products), and in de-ionzed water (viscosity 0.89 cSt; specific gravity 980 kg/m$^3$; SoS 1480 m/s). Water is the best US couplant among all not only because our transducers have been optimized for water immersion applications like biological tissue imaging, but also because water attenuation (0.97 dB/mm at 50 MHz) for US wave is the least among these four couplants. The mineral oil is the worst because it attenuates 20.62 dB/mm for 50 MHz US wave. Between 2-cSt and 0.65-cSt silicone oil we did not choose 0.65-cSt because in this viscosity range silicone oil is volatile in air at room temperature. The 2-cSt silicone oil though has an US attenuation of 5 dB/mm, we manage to mitigate the attenuation by using another de-ionized water bag to couple the RThAM wave generated from biological sample.

Lastly the acoustic impedance difference between de-ionized water/tissue and 2 cSt oil is only 80%, suggesting a negligible transmission loss of 0.83 dB for one transmission. Given tissue-oil and oil-water interfaces, the total transmission loss due to acoustic impedance mismatching would be 1.66 dB. As a result, if given a RThAM wave generated inside a tissue and later reached the surface, assuming the oil path is 1 mm and water/tissue path in sum is 5 mm (the focus of transducer is at 6 mm), the total loss before the RThAM signal is detected by US transducer, is 1.66 dB + 0.97 dB/mm × 5 mm + 5 dB/mm × 1 mm = 11.51 dB which is far less than the 31.66 dB loss when using 2-cSt oil only for US coupling. As also illustrated in table S1, pure oil coupling induces 38.61-dB total loss, while pure water coupling induces 43.89-dB total loss, among which the hybrid coupling solution demonstrates 20.95-dB total loss—the least among the three coupling modes.

To evaluate the effect of coupling methods in RThAM images, we also characterized the imaging resolution using a NaCl-soaked suture with a diameter of 50 μm, as shown in figs. S3 (A and B). Despite the overall low image contrast, we found that contrast along suture varied by <6 dB and that the narrowest width of suture appeared to be ~50 μm, while in the thicker oil the suture appeared to be ~100 μm in size. This result implies that there is only little difference between the system coupling configurations for resolution characterization if the oil path is <1 mm, justifying the use of water-coupled 25-ohm TxLine to characterize hybrid coupled RThAM imaging resolution. A longer path of silicone oil may deteriorate the resolution of RThAM. However, due to the short path of oil between the sample and water couplant, we did not see obvious effects in the zebrafish embryo sample, in which fine features <38 μm in size are visible in the yolk region (Fig. 2D). Similar fine structures (45 μm) were also observed in fig. S4. In zebrafish larvae measurements, due to the thinner size of the sample, the oil path may increase, resulting in a degradation of resolution. This is why in these experiments the sample bed was brought closer to the water bag so that the oil path is smaller than 1 mm. We therefore considered the difference negligible in resolution between hybrid oil/water coupling and pure water coupling.

## Note S3. Skin depth of RF energy into copper

One might ask why copper wire of 50 μm in diameter can give in RThAM image a resolution characterization found to be 23 μm axial and 33 μm lateral resolution in RThAM 50 MHz configuration (Fig. 1). Figure S1G shows a relation between skin depth in copper along frequency of RF energy. Keeping second harmonic thermoacoustic generation in mind, the RF absorption at $f_{RF}$ in conductive matter gives rise to thermoacoustic/RThAM wave of $f_{RThAM} = 2 \times f_{RF}$. If we simplified the detection model, a 50 MHz central frequency transducer detects a RThAM signal of $f_{RThAM} = 50$ MHz. This means the RThAM signal is induced due to a conductive absorption of the 25-MHz RF energy. The layer that absorbs has a thickness of 13 μm, meaning reaching at this depth the RF field strength decreases to 1/e and RF energy to 1/$e^2$. In contrast, the apparent lateral FWHM is a result of the cylindrical shape of the copper wire and the limited acceptance angle of the US transducer.

## Note S4. RThAM 100 MHz setup and characterization

Figure S2 illustrates the performance in terms of imaging resolution and signal-to-noise ratio (SNR), measured from a pair of copper wires (Ø50 μm) using transducer of 100 MHz central frequency (spherically focused; focus 1.5 mm; diameter 1.5 mm; HFM18, Sonaxis). Figure S2 (A and B) show the *xy* and *yz* images of the copper, respectively. Some signal from the background area could be the instant glue we applied to fix the position of copper wire sample. Figure S2C shows the profiles of lines in the *yz* image which demonstrates the achieved lateral FWHM of 16 μm and axial FWHM of 7 μm. Figure S2D is a temporal sequence of maximum RThAM amplitude showing the 28-dB SNR achieved and the signal frequency components up to 150 MHz. This experiment shows that the resolution of RThAM imaging is scalable and determined only by the applied RF pulse width, $f$-number and the detection bandwidth of transducer. But before applying RThAM 100 MHz to biological studies, US attenuation in the detection acoustic path would have to be reduced to <10 dB with proper design. The energy coupling element used for this experiment is a 25-ohm open TxLine with de-ionized water as dielectrics (6-mm dielectric gap and 3.5-mm conductor width). The wide gap and polar dielectric medium have substantially reduced the RF field strength (table S1). We tried to image biological samples with this TxLine with 50-MHz transducer but failed to obtain RThAM signals.

In current work, we chose to work with 50 MHz instead in order to guarantee substantial deposition of nanosecond pulsed RF energy offered by silicone oil dielectric, which attenuate US wave at 100 MHz by 20 dB/mm (fig. S1F). But as a result, the total loss of using the optimal hybrid oil/water coupling for RThAM 100 MHz is 49.44 dB (table S1) and thus not applicable for biological imaging experiments. We noticed that the zebrafish larvae images [Fig. 2 (I to K) and fig. S5 (E and F)] seemed worse in resolution than that of embryos [Fig. 2 (A to G) and fig. S4 (A to D)]. We attribute the reason to dispersive attenuation due to longer path of silicone oil (which can be adjusted using the sample bed to keep oil path <1 mm) for the case of larvae than for the case of embryos because larvae are smaller in thickness than embryos thus inducing a longer silicone oil gap between water bag and larvae attenuating more severely the thermoacoustic waves.

## Note S5. Acoustic velocity mismatch in oil/water hybrid coupling and reconstruction

We choose an SoS during reconstruction that maximizes images quality by minimizing the influence of acoustic velocity mismatch on image reconstruction. Acoustic velocity mismatch can cause refraction and has been demonstrated (*52, 53*) to induce reconstruction errors in localization, dimensions (smearing and deformation), by creating artefacts, and reducing imaging contrast and resolution, if the velocity mismatch is large or the acoustic paths are long. The effects are significant as well when the SoS varies with detection angle, such as in concaved array detection (*52, 53*), which relies on an SoS map to calculate the distance matrix and sum up the signals accordingly. An incorrect assumption of the SoS could create artefacts that do not exist in sample. In the case of RThAM the velocity mismatch appears large (931 m/s for silicone oil, and 1480 m/s for water), but the oil acts as a layer (<1 mm) between the sample (<1 mm) and water couplant (5 mm). However, the oil path and the sample thickness are very small compared to the water path. Informed by our previous work (*52*), we tried and selected a uniform SoS that is just below that of water, whereby the highest resolution and contrast reconstruction is obtained. In effect, we considered the effect of acoustic velocity mismatch insignificant. However, for higher image quality, precision in quantitative measurements, the acoustic velocity mismatch will have to be considered in a priori reconstructions using SoS and structural information (*53, 54*).

## Note S6. Effects of polarized excitation field on RThAM resolution and contrast

We expect the resolution to be symmetric in lateral plane because RThAM resolution is acoustically limited as conventional optoacoustic mesoscopy (*30, 41*). However, for longitudinal absorbers that are thin and long such as muscle or neural fibers, the polarized electric field would represent the contrast differently depending on the relative orientation of the fibers to the polarization of the field. Such asymmetric contrast can be understood at the level of charge carriers. For aligned orientation, the charge carriers would be accelerated by the RF field for longer distance along the fiber, i.e., larger converted and absorbed kinetic energy, while for the orientation perpendicular to the field polarization the absorbed RF energy is minimum. Future applications and interpretation of the RThAM contrast would need to consider this asymmetry effect.

To confirm, we have made another measurement using copper wire of 100 μm in diameter (fig. S3, C to E). For such experiments carbon fibers are interesting but we did not use carbon fiber (5–10 μm diameter) because its diameter is too small for current RThAM 50 MHz setup and the corresponding high central frequency US (~200 MHz) attenuates too severely for RThAM 100 MHz in hybrid oil/water coupling. Upon improvements in excitation energy density and acoustic coupling efficiency, carbon fiber should serve as a standard resolution target for thermoacoustic microscopy. The copper phantom results shown in fig. S3 (C to E) confirmed the homogeneous in-plane resolution, which is limited by acoustic diffraction and scanning step of the used transducer. The size (100 μm) of copper wires was correctly represented in

RThAM image for both orientation along $x$ and $y$ axis. As expected, the image showed clearly higher contrast from the wire orientation that is parallel to the field polarization compared to the perpendicular orientation.

# Supplementary Table

**Table S1. Coupling mode comparison: pure oil, pure water, hybrid oil/water at 50 and 100 MHz assuming same dielectric gap and ideal impedance matching.**

| **Coupling method** | **Permittivity** $\varepsilon_r$ | **Polarization induced net field energy decrease** $1/\varepsilon_r^2$ | **US trans. loss at interface(s)** | **100 MHz US attenuation** dB/mm × length | **100 MHz Total attenuation** | **50 MHz US attenuation** dB/mm × length | **50 MHz Total attenuation** |
|---|---|---|---|---|---|---|---|
| **Pure oil** | 2.45 | -7.78 dB | -0.83 dB | -20×6<br>= -120 dB | **-128.61 dB** | -5×6 mm<br>= -30 dB | **-38.61 dB** |
| **Pure water** | 80.1 | -38.07 dB | 0 | -4×6 mm<br>= -24 dB | **-62.07 dB** | -0.97×6 mm<br>= -5.82 dB | **-43.89 dB** |
| **Hybrid oil/water** | 2.45 | -7.78 dB | -0.83×2 dB | -4×5 - 20×1<br>= -40 dB | **-49.44 dB** | -0.97×5 - 5×1<br>= -11.51 dB | **-20.95 dB** |

# Supplementary Figure

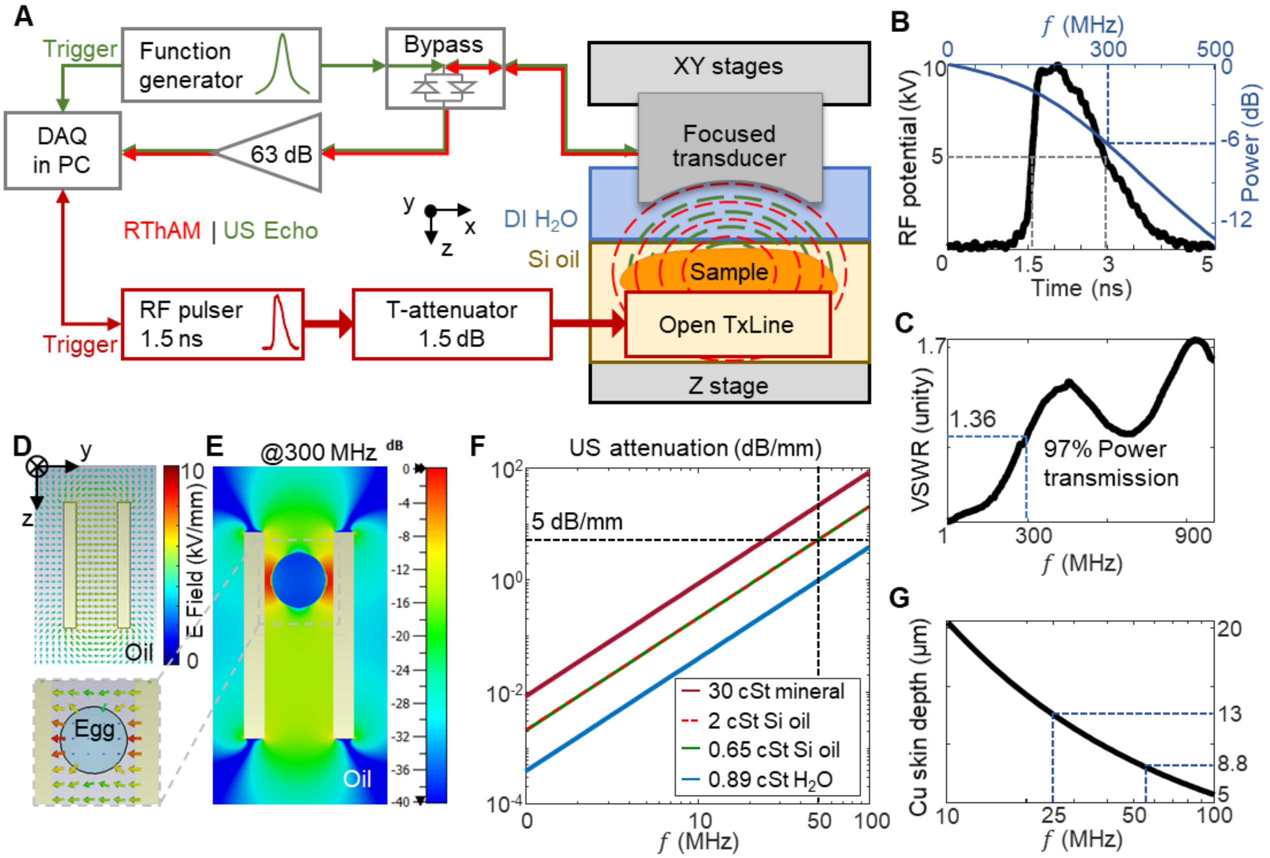

**Fig. S1. Schematic and characteristics of RThAM setup.** (**A**) Diagram of the RThAM setup. RF pulser generates 5–10 kV, 1.5 ns pulses which are coupled via coaxial cable to the sample in between the open TxLine. Conductive sample that absorbs the RF energy, generates acoustic wave (RThAM signal; dashed red arcs) due to thermoacoustic effect. The RThAM waves are coupled by de-ionized water (DI $H_2O$) to a spherically focused US transducer. The RThAM signal is amplified by a 63-dB amplifier and digitized by a data acquisition card (DAQ) in a personal computer (PC). The DAQ is triggered by either the RF pulser or function generator used in active US imaging. The PC synchronizes the setup, scans the stages to perform raster scan in the *xy* plane, stores and reconstructs the images. The custom-built bypass circuit is inserted to allow for ultrasonography using function generator exciting US emission in transducer. (**B**) A profile of RF pulse (black) showing the pulse width of 1.5 ns. The Fourier transform of RF pulse (blue) showing -6 dB cut-off frequency at 300 MHz. (**C**) The measured VSWR with a sample installed in the open TxLine to show the matched impedance for RF energy transmission below 300 MHz. (**D** and **E**) The EM simulation results at 300 MHz showing (**D**) E-field strength distribution in oil couplant without sample and (**E**) with the 'Egg' sample (permittivity of 80.1; conductivity 1 S/m) installed. (**F**) US attenuation below 100 MHz at room temperature in couplants with different viscosity: 30-cSt mineral oil, 2- and 0.65-cSt silicone oil, and 0.89-cSt water. At 50 MHz, US attenuation in silicone oil is 5 dB/mm, and in water is less than 1 dB/mm. (**G**) Skin depth in copper (Cu) of RF below 100 MHz. At 25 MHz, corresponding to 50-MHz RThAM signal, the skin depth is 13 μm (8.8 μm for RF at 54.5 MHz) beyond which only $1/e^2$ energy is left.

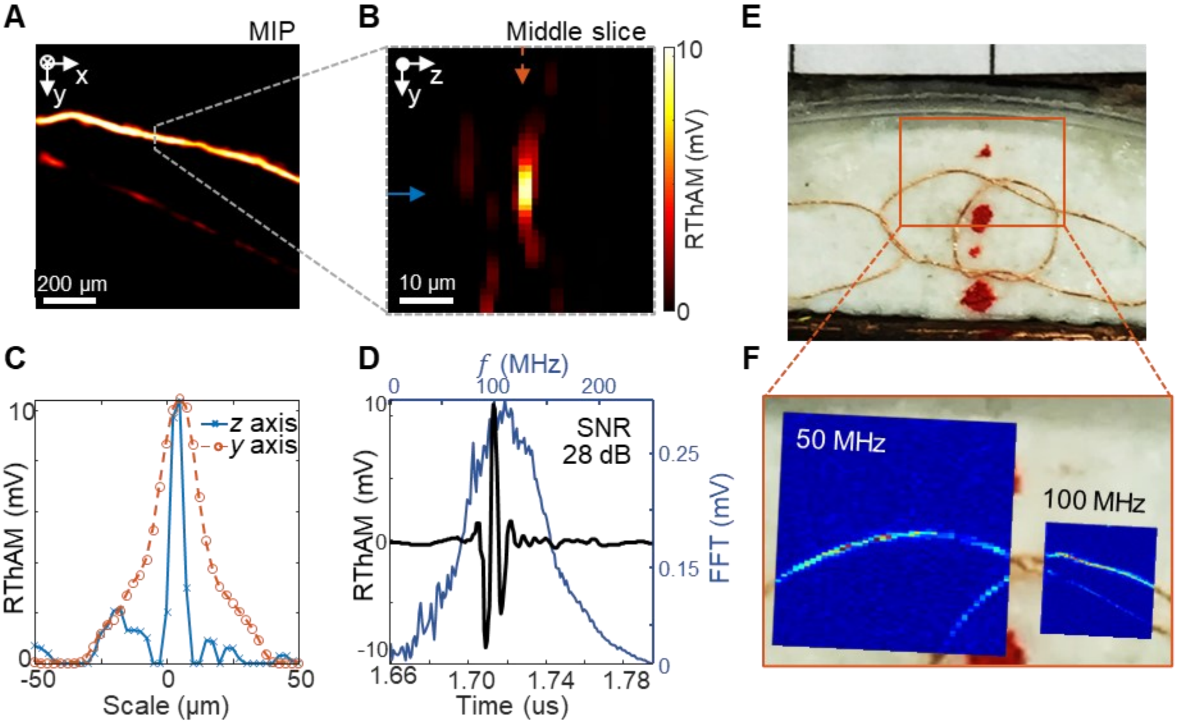

**Fig. S2. RThAM 100 MHz performance characterization.** (**A** and **B**) RThAM image of a pair of ⌀ 50 µm copper wires in the *xy* plane (**A**) and in the *yz* plane (**B**). Signals from background could be a result from the instant glue applied to keep the wires in position. The dotted grey line in (A), indicates the cross-sectional *yz* image shown in (B). Scale bar in (A) is 200 µm and in (B) 10 µm. The solid blue and dashed orange arrows in (B) indicates the *z*-axial and *y*-axial profile shown in (C), respectively. (**C**) 7 µm axial resolution and 16 µm lateral resolution shown by the *z*-axis (solid blue with cross marker) and *y*-axis (dashed orange with circle marker) profiles along the lines indicated in (B), respectively. (**D**) A temporal signal (black) of 28 dB signal-to-noise ratio and its Fourier transform (blue) showing frequency components and central frequency at 109 MHz. (**E** and **F**) A photograph of the copper phantom used for resolution characterization experiments (E) with RThAM 50 MHz image (jet colormap version of Fig. 1B) overlaid on the left and RThAM 100 MHz [jet colormap version of (A)] on the right in (F). Photo Credit: Yuanhui Huang, TUM.

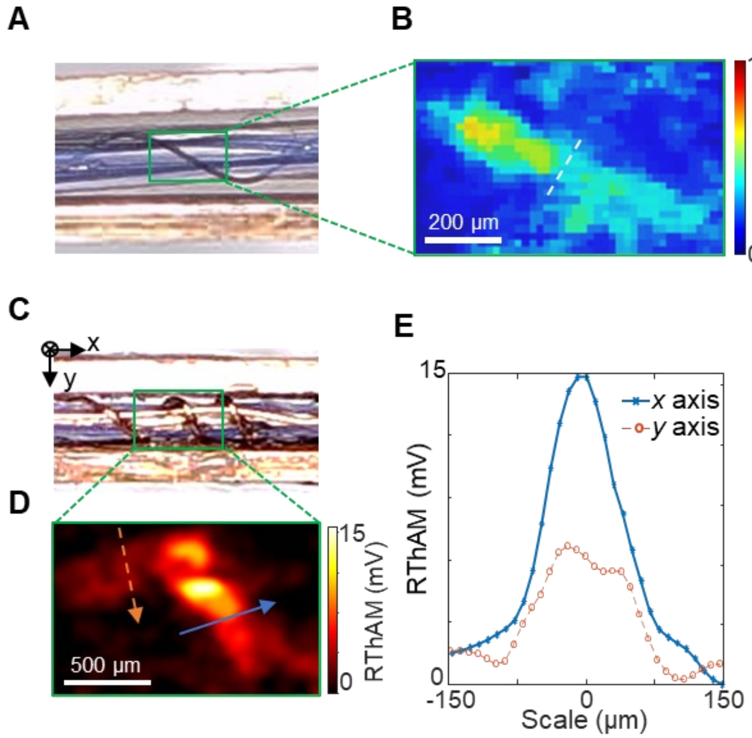

**Fig. S3. Saline-soaked suture and copper in RThAM 50 MHz using hybrid oil/water coupling.** (**A** and **B**) A suture (polyamide ⌀50 µm) wrapped around a tubing (⌀800 µm) showing the in-plane resolution in hybrid oil/water coupling. The suture phantom was soaked in 10% w/v NaCl solution [1.7 mM; ~28.86 S/m according to Widodo *et al.* (*55*)] for two hours and placed wet in the open transmission line. (**A**) An optical photo showing the imaged suture extending into the sample space, with central segment affected by a shorter oil path. (**B**). The RThAM image showing the small variations in the contrast of the suture. The slight background contrast may result from the residual NaCl saline on the surface of tubing. Note that the narrowest part (dashed white line) of the phantom was measured to be ~50 µm in width. (**C** to **E**) A coil of copper wire (⌀100 µm) wrapped around tubing (⌀600 µm) showing the polarization effect of the electric field depending on the orientation of sample. (**C**) An optical photo showing the imaged "cross" in the copper coil phantom in hybrid oil/water coupling. (**D**). The RThAM image showing the cross with similar size but different contrast intensity because of the polarized excitation field. The arrows indicate the profiles shown in (E). (**E**) Profiles along arrows indicated in (B) showing the relative contrast and apparent size of sample with orientations perpendicular (*x* axis; solid blue) and parallel (*y* axis; dotted orange) to the field polarization. Photo Credit: Yuanhui Huang, TUM.

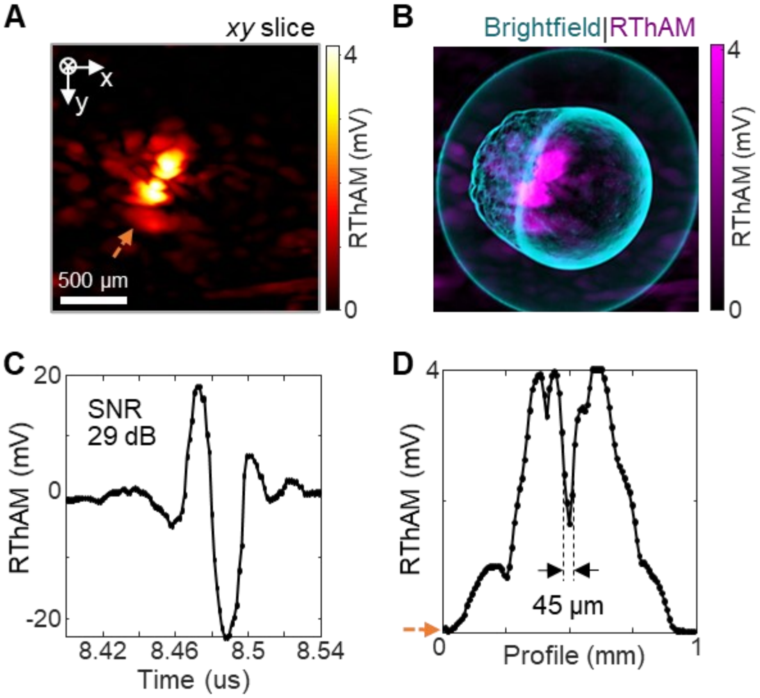

**Fig. S4. RThAM cross-section in depth and profile.** (**A**) A cross-sectional RThAM image of the embryo four hpf shown in Fig. 2 (E to H). The image is formed by using a middle slice (200 µm) in the *z*-axis direction along arrows indicated in Fig. 2H. Dotted orange arrow indicates the profile analyzed in (D). (**B**) An overlay of RThAM image slice onto the microphotograph of the embryo showing strong RF absorption on the interface of blastomeres and the yolk. (**C**) An example RThAM signal, showing the achieved 29-dB SNR in cells. The signal was taken from the maximum pixel in Fig. 2F. (**D**) The line profile indicated in (A), showing the relative RF absorption in the embryo and the resolution power down to 45 µm.

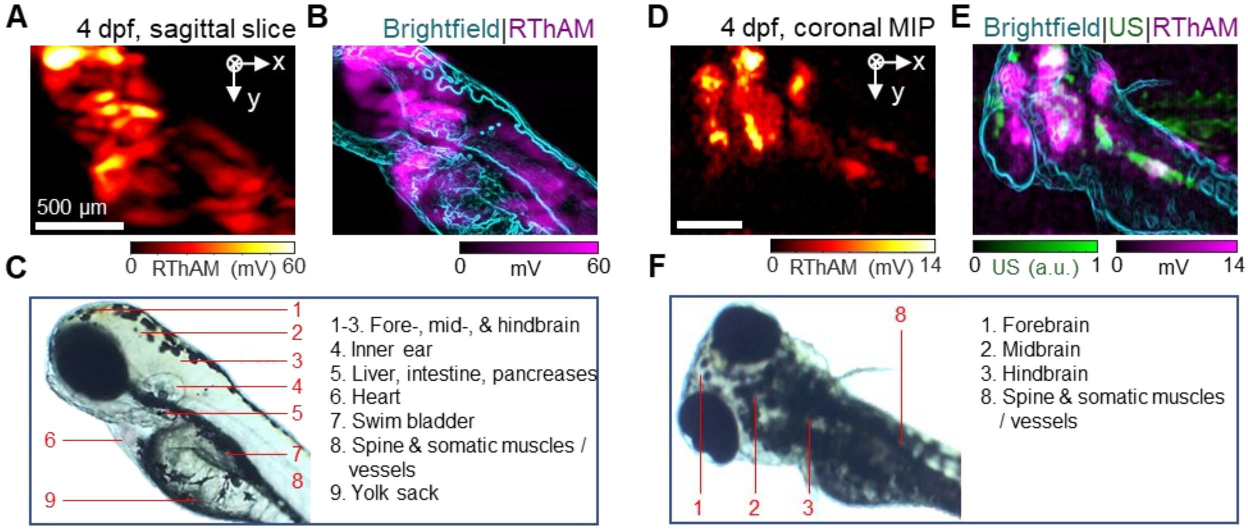

**Fig. S5. RThAM imaging on wild type zebrafish larvae of four dpf.** (**A** to **C**) Larva in the sagittal position. (**A**) RThAM slice (~150 µm in thickness) at the depth of the spinal cord in a hot map of the zebrafish in sagittal view showing the major contrast from the head, abdomen, and trunk region. (**B**) An overlay of the RThAM slice (magenta) onto the reflection-mode optical image (bright field; edge filtered; cyan). (**C**) A bright-field microphotograph of the zebrafish larva with annotation of major anatomical features. (**D** to **F**) Larva in the coronal (see 3D distribution in movie S3) position. (**D**) The RThAM MIP in hot map of the zebrafish in coronal position showing the major contrast from the head, abdomen, and trunk region. (**E**) An overlay of the RThAM MIP (magenta), US pulse-echo image (green), and the bright field microphotograph (cyan, edge filtered) showing coregistered features in hybrid appearance. The whitish areas are a result of blending magenta and green, i.e., the overlapping area between RThAM and US contrast. (**F**) Bright-field microphotograph of the larva in coronal position with annotation of major anatomical features in the view. Scale bars are 500 µm.

## Supplementary Movie Caption

**Movie S1. RThAM 3D of zebrafish embryo at 1 cell stage.** Dual-mode RThAM/US imaging of the same sample as Fig. 2 (A to D) at 0.5 hpf. The mesh sphere is added manually for localization purpose using ImageJ. The flat object is the polyethylene film used as water bag. The simultaneous dual-mode 3D image renders RThAM contrast in red and US pulse-echo contrast in green.

**Movie S2. RThAM 3D of zebrafish embryo at 512 cell stage.** Dual-mode RThAM/US imaging of the same sample as Fig. 2 (E to H) at 4 hpf. The mesh sphere is added manually for localization purpose using ImageJ. The flat object is the polyethylene film used as water bag. The simultaneous dual-mode 3D image renders RThAM contrast in red and US pulse-echo contrast in green.

**Movie S3. RThAM 3D of wildtype zebrafish larva at 4 dpf.** Dual-mode RThAM/US imaging of the same sample as supplementary fig. S5 (D to F). The simultaneous dual-mode 3D image renders RThAM contrast in red and US pulse-echo contrast in green. Some US contrast can also be seen from the exposed part of sample bed (tubing used to support the sample), and from copper plates of open transmission line.

## REFERENCES AND NOTES

1. M. Dressel, M. Scheffler, Verifying the Drude response. *Ann. Phys.* **15**, 535–544 (2006).
2. P. Grasland-Mongrain, C. Lafon, Review on biomedical techniques for imaging electrical impedance. *IRBM* **39**, 243–250 (2018).
3. J. Matthias, J. Maul, R. Noster, H. Meinl, Y.-Y. Chao, H. Gerstenberg, F. Jeschke, G. Gasparoni, A. Welle, J. Walter, K. Nordström, K. Eberhardt, D. Renisch, S. Donakonda, P. Knolle, D. Soll, S. Grabbe, N. Garzorz-Stark, K. Eyerich, T. Biedermann, D. Baumjohann, C. E. Zielinski, Sodium chloride is an ionic checkpoint for human $T_H2$ cells and shapes the atopic skin microenvironment. *Sci. Transl. Med.* **11**, eaau0683 (2019).
4. D. Haemmerich, S. T. Staelin, J. Z. Tsai, S. Tungjitkusolmun, D. M. Mahvi, J. G. Webster, In vivo electrical conductivity of hepatic tumours. *Physiol. Meas.* **24**, 251–260 (2003).
5. V. D. Schepkin, F. C. Bejarano, T. Morgan, S. Gower-Winter, M. Ozambela Jr, C. W. Levenson, In vivo magnetic resonance imaging of sodium and diffusion in rat glioma at 21.1 T. *Magn. Reson. Med.* **67**, 1159–1166 (2012).
6. D. M. Gordon, S. R. Ash, Lack of correlation of glucose levels in filtered blood plasma to density and conductivity measurements. *ASAIO J.* **55**, 227–230 (2009).
7. M. Schaefer, W. Gross, J. Ackemann, M. M. Gebhard, The complex dielectric spectrum of heart tissue during ischemia. *Bioelectrochemistry* **58**, 171–180 (2002).
8. T. J. Jentsch, C. A. Hubner, J. C. Fuhrmann, Ion channels: Function unravelled by dysfunction. *Nat. Cell Biol.* **6**, 1039–1047 (2004).
9. F. Manoni, L. Fornasiero, M. Ercolin, A. Tinello, M. Ferrian, S. Valverde, G. Gessoni, Laboratory diagnosis of renal failure: Urine conductivity and tubular function. *Minerva Urol. Nefrol.* **61**, 17–20 (2009).
10. E. Neher, B. Sakmann, Single-channel currents recorded from membrane of denervated frog muscle fibres. *Nature* **260**, 799–802 (1976).
11. A. L. Hodgkin, A. F. Huxley, Propagation of electrical signals along giant nerve fibres. *Proc. R. Soc. Lond B* **140**, 177–183 (1952).
12. J. Abbott, T. Ye, K. Krenek, R. S. Gertner, S. Ban, Y. Kim, L. Qin, W. Wu, H. Park, D. Ham, A nanoelectrode array for obtaining intracellular recordings from thousands of connected neurons. *Nat. Biomed. Eng.* **4**, 232–241 (2019).

13. P. K. Hansma, B. Drake, O. Marti, S. A. Gould, C. B. Prater, The scanning ion-conductance microscope. *Science* **243**, 641–643 (1989).

14. X. D. Cui, A. Primak, X. Zarate, J. Tomfohr, O. F. Sankey, A. L. Moore, T. A. Moore, D. Gust, G. Harris, S. M. Lindsay, Reproducible measurement of single-molecule conductivity. *Science* **294**, 571–574 (2001).

15. R. H. Bayford, Bioimpedance tomography (electrical impedance tomography). *Annu. Rev. Biomed. Eng.* **8**, 63–91 (2006).

16. E. Boto, N. Holmes, J. Leggett, G. Roberts, V. Shah, S. S. Meyer, L. D. Muñoz, K. J. Mullinger, T. M. Tierney, S. Bestmann, G. R. Barnes, R. Bowtell, M. J. Brookes, Moving magnetoencephalography towards real-world applications with a wearable system. *Nature* **555**, 657–661 (2018).

17. N. Vogt, Voltage sensors: Challenging, but with potential. *Nat. Methods* **12**, 921–924 (2015).

18. E. S. Boyden, F. Zhang, E. Bamberg, G. Nagel, K. Deisseroth, Millisecond-timescale, genetically targeted optical control of neural activity. *Nat. Neurosci.* **8**, 1263–1268 (2005).

19. W. Akemann, H. Mutoh, A. Perron, J. Rossier, T. Knöpfel, Imaging brain electric signals with genetically targeted voltage-sensitive fluorescent proteins. *Nat. Methods* **7**, 643–649 (2010).

20. G. Cao, J. Platisa, V. A. Pieribone, D. Raccuglia, M. Kunst, M. N. Nitabach, Genetically targeted optical electrophysiology in intact neural circuits. *Cell* **154**, 904–913 (2013).

21. Y. Gong, M. J. Wagner, J. Zhong Li, M. J. Schnitzer, Imaging neural spiking in brain tissue using FRET-opsin protein voltage sensors. *Nat. Commun.* **5**, 3674 (2014).

22. V. S. Sohal, F. Zhang, O. Yizhar, K. Deisseroth, Parvalbumin neurons and gamma rhythms enhance cortical circuit performance. *Nature* **459**, 698–702 (2009).

23. H. J. Lee, D. Zhang, Y. Jiang, X. Wu, P.-Y. Shih, C.-S. Liao, B. Bungart, X.-M. Xu, R. Drenan, E. Bartlett, J.-X. Cheng, Label-free vibrational spectroscopic imaging of neuronal membrane potential. *J. Phys. Chem. Lett.* **8**, 1932–1936 (2017).

24. R. Schirhagl, K. Chang, M. Loretz, C. L. Degen, Nitrogen-vacancy centers in diamond: Nanoscale sensors for physics and biology. *Annu. Rev. Phys. Chem.* **65**, 83–105 (2014).

25. C.-C. Fu, H.-Y. Lee, K. Chen, T.-S. Lim, H.-Y. Wu, P.-K. Lin, P.-K. Wei, P.-H. Tsao, H.-C. Chang, W. Fann, Characterization and application of single fluorescent nanodiamonds as cellular biomarkers. *Proc. Natl. Acad. Sci. U.S.A.* **104**, 727–732 (2007).

26. N. K. Nikolova, Microwave imaging for breast cancer. *IEEE Microw. Mag.* **12**, 78–94 (2011).

27. P. Wang, Z. Li, P. Liu, Y. Pei, Super resolution in depth for microwave imaging. *Appl. Phys. Lett.* **115**, 044101 (2019).
28. T. Voigt, U. Katscher, O. Doessel, Quantitative conductivity and permittivity imaging of the human brain using electric properties tomography. *Magn. Reson. Med.* **66**, 456–466 (2011).
29. T. Bowen, Radiation-induced thermoacoustic soft tissue imaging, in *Proceedings of the 1981 Ultrasonics Symposium*, Chicago, IL, USA, 14 to 16 October 1981.
30. M. Omar, J. Aguirre, V. Ntziachristos, Optoacoustic mesoscopy for biomedicine. *Nat. Biomed. Eng.* **3**, 354–370 (2019).
31. R. A. Kruger, K. D. Miller, H. E. Reynolds, W. L. Kiser Jr., D. R. Reinecke, G. A. Kruger, Breast cancer in vivo: Contrast enhancement with thermoacoustic CT at 434 MHz-feasibility study. *Radiology* **216**, 279–283 (2000).
32. M. Omar, S. Kellnberger, G. Sergiadis, D. Razansky, V. Ntziachristos, Near-field thermoacoustic imaging with transmission line pulsers. *Med. Phys.* **39**, 4460–4466 (2012).
33. L. Nie, D. Xing, Q. Zhou, D. Yang, H. Guo, Microwave-induced thermoacoustic scanning CT for high-contrast and noninvasive breast cancer imaging. *Med. Phys.* **35**, 4026–4032 (2008).
34. C. C. Johnson, A. W. Guy, Nonionizing electromagnetic wave effects in biological materials and systems. *Proc. IEEE* **60**, 692–718 (1972).
35. D. Razansky, S. Kellnberger, V. Ntziachristos, Near-field radiofrequency thermoacoustic tomography with impulse excitation. *Med. Phys.* **37**, 4602–4607 (2010).
36. Y. Huang, S. Kellnberger, G. Sergiadis, V. Ntziachristos, Blood vessel imaging using radiofrequency-induced second harmonic acoustic response. *Sci. Rep.* **8**, 15522 (2018).
37. M. S. Aliroteh, A. Arbabian, Microwave-induced thermoacoustic imaging of subcutaneous vasculature with near-field RF excitation. *IEEE Trans. Microw. Theory Tech.* **66**, 577–588 (2018).
38. K. Tamarov, M. Gongalsky, L. Osminkina, Y. Huang, M. Omar, V. Yakunin, V. Ntziachristos, D. Razansky, V. Timoshenko, Electrolytic conductivity-related radiofrequency heating of aqueous suspensions of nanoparticles for biomedicine. *Phys. Chem. Chem. Phys.* **19**, 11510–11517 (2017).
39. S. Gabriel, R. W. Lau, C. Gabriel, The dielectric properties of biological tissues: III. Parametric models for the dielectric spectrum of tissues. *Phys. Med. Biol.* **41**, 2271–2293 (1996).
40. R. Buchner, J. Barthel, J. Stauber, The dielectric relaxation of water between 0°C and 35°C. *Chem. Phys. Lett.* **306**, 57–63 (1999).

41. J. Aguirre, M. Schwarz, N. Garzorz, M. Omar, A. Buehler, K. Eyerich, V. Ntziachristos, Precision assessment of label-free psoriasis biomarkers with ultra-broadband optoacoustic mesoscopy. *Nat. Biomed.* **1**, 0068 (2017).

42. K. Kawakami, E. E. Patton, M. Orger, *Zebrafish: Methods and Protocols, Methods in Molecular Biology* (Methods and Protocols Second Edition, Springer, 2016), 366 pp.

43. P. A. Hasgall, F. Di Gennaro, C. Baumgartner, E. Neufeld, B. Lloyd, M. C. Gosselin, D. Payne, A. Klingenböck, N. Kuster, IT'IS Database for thermal and electromagnetic parameters of biological tissues. Version 4.0 (2018).

44. C. Lou, S. Yang, Z. Ji, Q. Chen, D. Xing, Ultrashort microwave-induced thermoacoustic imaging: A breakthrough in excitation efficiency and spatial resolution. *Phys. Rev. Lett.* **109**, 218101 (2012).

45. S. Liu, R. Zhang, Y. Luo, Y. Zheng, Magnetoacoustic microscopic imaging of conductive objects and nanoparticles distribution. *J. Appl. Phys.* **122**, 124502 (2017).

46. X. Feng, F. Gao, R. Kishor, Y. Zheng, Coexisting and mixing phenomena of thermoacoustic and magnetoacoustic waves in water. *Sci. Rep.* **5**, 11489 (2015).

47. X. H. Feng, F. Gao, Y. J. Zheng, Magnetically mediated thermoacoustic imaging toward deeper penetration. *Appl. Phys. Lett.* **103**, 083704 (2013).

48. W. Luo, Z. Ji, S. Yang, D. Xing, Microwave-pumped electric-dipole resonance absorption for noninvasive functional imaging. *Phys. Rev. Appl.* **10**, 024044 (2018).

49. J. Li, A. Chekkoury, J. Prakash, S. Glasl, P. Vetschera, B. Koberstein-Schwarz, I. Olefir, V. Gujrati, M. Omar, V. Ntziachristos, Spatial heterogeneity of oxygenation and haemodynamics in breast cancer resolved in vivo by conical multispectral optoacoustic mesoscopy. *Light Sci. Appl.* **9**, 57 (2020).

50. Y. Li, L. Li, L. Zhu, K. Maslov, J. Shi, P. Hu, E. Bo, J. Yao, J. Liang, L. Wang, L. V. Wang, Snapshot photoacoustic topography through an ergodic relay for high-throughput imaging of optical absorption. *Nat. Photonics* **14**, 164–170 (2020).

51. M. P. Murrell, M. E. Welland, S. J. O'Shea, T. M. H. Wong, J. R. Barnes, A. W. McKinnon, M. Heyns, S. Verhaverbeke, Spatially resolved electrical measurements of $SiO_2$ gate oxides using atomic force microscopy. *Appl. Phys. Lett.* **62**, 786–788 (1993).

52. X. L. Deán-Ben, V. Ntziachristos, D. Razansky, Effects of small variations of speed of sound in optoacoustic tomographic imaging. *Med. Phys.* **41**, 073301 (2014).

53. H. Yang, D. Jüstel, J. Prakash, V. Ntziachristos, Modeling the variation in speed of sound between couplant and tissue improves the spectral accuracy of multispectral optoacoustic tomography. *Proc. SPIE* **10890**, 1089027 (2019).

54. H. Yang, D. Jüstel, J. Prakash, A. Karlas, A. Helfen, M. Masthoff, M. Wildgruber, V. Ntziachristos, Soft ultrasound priors in optoacoustic reconstruction: Improving clinical vascular imaging. *Photoacoustics* **19**, 100172 (2020).

55. C. S. Widodo, H. Sela, D. R. Santosa, The effect of NaCl concentration on the ionic NaCl solutions electrical impedance value using electrochemical impedance spectroscopy methods. *AIP Conf. Proc.* **2021**, 050003 (2018).

56. R. Feymann, R. B. Leighton, M. Sands, *The Feynman Lectures on Physics* (Addison-Wesley, 1965).